ORCA – Online Research @ Cardiff

Pizzutilo, Enrico, Freakley, Simon J., Cherevko, Serhiy, Venkatesan, Sriram, Hutchings, Graham John , Liebscher, Christian H., Dehm, Gerhard and Mayrhofer, Karl J. J. 2017. Gold-palladium bimetallic catalyst stability: consequences for hydrogen peroxide selectivity. ACS Catalysis 7 , pp. 5699-5705. 10.1021/acscatal.7b01447

Publishers page: http://dx.doi.org/10.1021/acscatal.7b01447

Gold-Palladium Bimetallic Catalyst Stability: Consequences for Hydrogen Peroxide Selectivity.

Enrico Pizzutilo[a*], Simon J. Freakley[b], Serhiy Cherevko[a,c], Sriram Venkatesan[d], Graham J. Hutchings[b], Christian H. Liebscher[d], Gerhard Dehm[d], Karl J. J. Mayrhofer[a,c,e*].

[a]Department of Interface Chemistry and Surface Engineering, Max-Planck-Institut für Eisenforschung GmbH, Max-Planck-Strasse 1, 40237 Düsseldorf, Germany

[b]Cardiff Catalysis Institute, School of Chemistry, Cardiff University, Main Building, Park Place, Cardiff, CF10 3AT

[c]Forschungszentrum Jülich, Helmholtz-Institute Erlangen-Nürnberg for Renewable Energy (IEK-11), Egerlandstr. 3, 91058 Erlangen, Germany

[d]Department of Structure and Nano-/ Micromechanics of Materials, Max-Planck-Institut für Eisenforschung GmbH, Max-Planck-Strasse 1, 40237 Düsseldorf, Germany

[e]Department of Chemical and Biological Engineering, Friedrich-Alexander-Universität Erlangen-Nürnberg, Egerlandstr. 3, 91058 Erlangen, Germany

KEYWORDS. Bimetallic catalysts, gold, palladium, hydrogen peroxide, electrocatalyst, degradation, stability.

ABSTRACT: During application, electrocatalysts are exposed to harsh electrochemical conditions, which can induce degradation. This work addresses the degradation of AuPd bimetallic catalysts used for the electrocatalytic production of hydrogen peroxide (H_2O_2) by oxygen reduction reaction (ORR). Potential dependent changes in the AuPd surface composition occur because the two metals have different dissolution onset potentials, resulting in catalyst dealloying. Using the scanning flow cell (SFC) with an inductively coupled plasma mass spectrometer (ICPMS), the simultaneous Pd and/or Au dissolution can be observed. Thereafter, three accelerated degradation protocols (ADPs), simulating different dissolution regimes, are employed to study the catalyst structure degradation on the nanoscale with identical location (IL-) TEM. When only Pd or both Au and Pd dissolve, the composition changes rapidly and the surface becomes enriched with Au as observed by cyclic voltammetry and elemental mapping. Such changes are mirrored by the evolution of electrocatalytic performances towards the H_2O_2 production. Our experimental findings are finally summarized in a dissolution/structure/selectivity mechanism providing a clear picture of the degradation of bimetallic catalyst used for H_2O_2 synthesis.

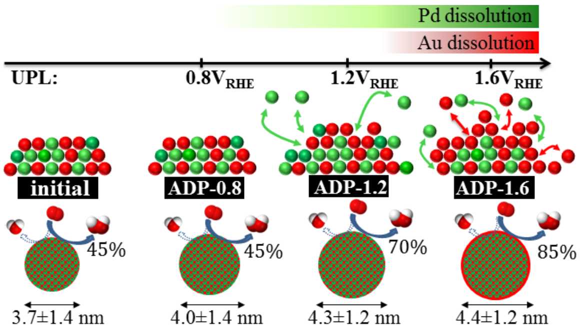

1 INTRODUCTION

Hydrogen peroxide (H_2O_2) is a green chemical oxidant that, for its potential impact on our society has been also listed as one of the most important chemical compounds [1]. Over 95% of the current global supply is produced using an indirect process involving sequential hydrogenation and oxidation of anthraquinones [2]. The anthraquinone process, despite being able to produce large quantities at high concentration is not considered "green" as 1) regeneration of the solution and impurity separation is required and 2) the obtained H_2O_2 is concentrated up to 70 wt% to reduce transportation costs [3]. This is feasible for applications in large industrial processes such as the pulp paper industry and bulk synthesis of organic compounds (i.e. propylene oxide), on the other hand it is inefficient for other smaller scale applications such as water-cleaning and disinfection for which typical concentration requirements are in the range of 2-8% [3,4]. Therefore, new approaches and catalysts to produce H_2O_2 on-site on a small scale need to be developed [5]. The idea of small scale production through heterogeneous catalysis dates back to 1939 as a first patent on production of H_2O_2 with Pd [2] opened the way to the field of "direct synthesis" in a catalytic reactor using H_2 and O_2 [4-7]. Nevertheless, safety issues related to the explosive region of H_2 and O_2 (5-95 vol%) limit practical uses [8]. The electrocatalytic production of H_2O_2 in a fuel cell [9-14] does not suffer from explosive gas environments as the two gases are provided separately to the cathode and anode and in addition, electrons can be collected through an external circuit. Several metals interacting weakly with O_2 (as Au, Hg, Ag) were shown to be able to reduce O_2 selectively to H_2O_2 [15,16]. Nevertheless, the rate is often low and high overpotentials (from the equilibrium of 0.69 V) are necessary. On the other hand, metals that interact strongly with oxygen (i.e. Pt, Pd) directly reduce O_2 to H_2O in a 4 electron process [17-20] and they only produce hydrogen peroxide if the surface is poisoned or covered with hydrogen [19]. Combining weakly and strongly interacting metals in homogeneous bimetallic catalysts can both improve the selectivity and maintain a high activity for the oxygen reduction reaction (ORR) to H_2O_2, as it was shown for Au-Pd [21-23] and Hg-Pt/Hg-Pd [24-26]. Furthermore the dispersion of the active metal (i.e. Pd) in a matrix of inactive metal (i.e. Au) was suggested in some studies to increase the overall selectivity [21], even though other works disagree [23].

Despite the promising introduction of such bimetallic electrocatalysts, their long-term stability needs to be considered [27]. Indeed, if they are to be used in a PEMFC they have to demonstrate enough stability to survive the harsh operational condition, especially during start-stop when the potential can reach 1.5 V_{RHE} [28]. Under operation, severe changes in surface composition due to metal migration [29], surface segregation [22], dissolution and dealloying [30-34] can dramatically affect the performance of such catalysts, significantly undermining the feasibility of the approach.

In this context, we present here a study on the stability of bimetallic Au-Pd catalysts. In this novel approach, we want to correlate the dissolution under various ADPs to the changes in the nanoparticle metal spatial distribution (both surface and bulk). Finally, the impact of such “degradation” on the ORR to H_2O_2 is also evaluated. The catalysts are characterized using various techniques such as inductively coupled plasma mass spectrometry (ICPMS), identical location transmission electron microscope (IL-TEM), high-resolution STEM-EDS and standard electrochemical techniques.

2 EXPERIMENTAL SECTION

2.1 NANOPARTICLES SYNTHESIS AND CHARACTERIZATION

The supported Au, AuPd and Pd nanoparticles were synthesized following a method described previously, consisting of a colloidal method [23] followed by nanoparticle immobilization onto XC72R Vulcan carbon (to yield a 10wt% metal loading). Once ready, the solution was filtered and the catalyst washed thoroughly (2 L H_2O); the dry catalyst powder is obtained after drying (16 h 120 °C).

The catalyst powder was used to prepare ink suspensions (in 18 MΩ·cm ultrapure water, UPW, from PureLab Plus system) ready to be “printed” onto the electrode. The theoretical molar ratio was confirmed by ICPMS for the as-prepared AuPd/C after dissolving the catalyst in boiling aqua regia (4 ml solution, from Merck, Suprapur). The same method was used to determine the remaining Pd content after degradation.

2.2 ELECTROCHEMICAL CHARACTERIZATION

All electrochemical measurements were performed using gas (Ar for the initial background and dissolution CVs or O_2 for the ORR) purged 0.1 M $HClO_4$ as supporting electrolyte. This was prepared from concentrated $HClO_4$ (Suprapur®, Merck) and UPW. Gamry Reference 600 potentiostats were used and controlled with the Gamry V6 Software or with a home-developed software based on Lab-View environment. A carbon rod was used as a counter electrode (CE), while the reference electrode (RE) was a commercial Ag/AgCl electrode (Metrohm). The potential shown in this work are all referred to the reversible hydrogen electrode (RHE) and the experiments are performed at room temperature.

The Ar background and the ORR curves are obtained via thin-film technique on a rotating ring–disc electrode (RRDE, commercial tip from Pine Instrument). 20 μL of ink were deposited on the glassy carbon disc (GC) obtaining a homogeneous film with a loading of 10 μg_{metal} cm^{-2} (disc area 0.196 cm^2). The material of the collector ring was Pt and the ring potential (E_r) was set at 1.0 V (1.28 V_{RHE}). At this potential, diffusion limited conditions for peroxide reduction and oxidation reaction (PROR) are reached. The collection efficiency (N) calculated from a simple 1 e^- reaction (hexacyanoferrate(III) reduction) was 0.21. A commercial MSR Rotator System with a Motor Controller (Pine Instrument Company) was used to rotate the electrode during the ORR reaction at a speed of 900 rpm if not else mentioned. The measurements were carried out in a three-compartment, three electrode Teflon cell [23] where the RE was hosted in a Tschurl modification (to separate it from the main compartment with a Nafion membrane) in order to avoid chloride contamination. The disc and ring currents (I_d and I_r) were measured (scan rate 0.05 V s^{-1}) after 1-10-50-100-1000 degradation CVs under different accelerated degradation protocols (ADPs). Three ADPs with a scan rate of 1 V s^{-1} were considered:

- ADP-0.8 consisting in 1000 CVs in the range [0.1-0.8] V_{RHE};
- ADP-1.2 consisting in 1000 CVs in the range [0.1-1.2] V_{RHE};
- ADP-1.6 consisting in 100 CVs in the range [0.1-1.6] V_{RHE}.

Palladium and gold dissolution of the Au/C, AuPd/C and Pd/C catalyst was studied with the scanning flow cell (SFC), whose aperture is of 0.01 cm^2. Approximately 2 ng of metal (20 ng with support) were printed onto GC electrodes using a drop-on-demand printer (Nano-PlotterTM 2.0, GeSim). The SFC was coupled with an on-line ICPMS (NexION 300X, Perkin Elmer) where the dissolved ^{197}Au and ^{106}Pd are analyzed and compared to internal standards for quantitative evaluation, as described in previous works [35]. The dissolution was measured during initial 900 s of the three ADPs (in this case with a 0.2 V s^{-1} scan rate).

2.3 TEM CHARACTERIZATION

The prepared catalyst ink was dispersed onto a lacey carbon film supported by a gold coated TEM finder grid. The prepared grid was used to perform identical location TEM (IL-TEM) [35]. Before and after ADP the particle size distribution in the same identical location was examined by scanning transmission electron microscopy (STEM) with a JEOL 2200FS TEM operating at 200 kV. The chemical composition and the elemental mapping investigation of single nanoparticles after ADPs were performed by energy dispersive spectroscopy (EDS). The Bruker Super-X windowless 4 quadrant silicon drift detector with a solid angle > 0.7 srad fitted in the C_s probe corrected FEI Titan Themis S/TEM operated at 300kV were used. The EDS measurements were performed in the STEM mode with the probe size of about 1 Å. A probe current of 70 pA for imaging and 0.5 pA for EDS, probe semi-convergence angle of 23.8 mrad, as well as inner- and outer semi-collection angle of the high angle annular dark-field (HAADF) detector of 73-352 mrad were used for imaging and STEM-EDS measurements.

3 RESULTS AND DISCUSSION

The AuPd/C employed in this study, as well as the reference Au/C and Pd/C, are synthesized through a sol-immobilization method and have a nominal metal loading of 10wt%. In our previous publication, we characterized the dissolution behavior of AuPd particles immobilized directly onto an electrode as a model system [30,31]. In particular, we showed that the difference in Pd and Au dissolution onset potentials (ca. 0.8 and 1.3 V_{RHE} respectively) between the alloyed AuPd nanoparticles and the pure Au and Pd counterparts is negligible. This is in contrast with other works reporting a stabilization effect (thus higher onset potential of dissolution) once small percentages of Au are present in the alloy [36]. In this study, we focus on the long-term electrochemical stability of AuPd/C as well as its structural changes and how these influence H_2O_2 production. Three different ADPs are considered (see experimental): ADP-0.8, ADP-1.2 and ADP-1.6. The latter is stopped after a lower amount of degradation cycles as the structure and electrochemical behavior was observed to change drastically under such harsh potential condition.

3.1 Au AND Pd DISSOLUTION AND EVOLUTION OF SURFACE COMPOSITION

Figure 1a reports the online potential dissolution profiles of Pd and Au measured by means of SFC-ICPMS during the first 800 s of the respective ADPs on the AuPd/C catalyst. As expected from the relative onset potentials, Pd dissolution occurs during the ADP-1.2, while Au dissolution is visible only under ADP-1.6. Interestingly, the Pd dissolution profiles after ca. 800 s of ADP-1.2 approaches the background signal, while the signal for ADP-1.6 is still high, as Au is also dissolving exposing fresh Pd on the surface of the nanoparticles. Evidence of the surface change induced by dissolution is supported by the CVs recorded in Ar saturated electrolytes (Figure 1b). Indeed, once the upper potential limit (UPL) is sufficiently high (above Au oxide formation [30], ca. 1.5 V_{RHE}) two distinct peaks are observable on the reverse scan: Pd oxide and Au oxide reduction. Note that for pure Pd/C and Au/C the peaks are at 0.55 V_{RHE} (Pd-O reduction) and 1.15 V_{RHE} (Au-O reduction) respectively, whereas for alloyed AuPd/C the reduction peak positions and relative charges (Table 1) of these two peaks are associated with the surface alloy composition [21,23,37-40]. In particular, the Pd-O reduction peak position in alloyed AuPd catalyst was shown to be shifted by ~200-300 mV to higher potentials [23,37], as a new phase is formed once Pd is alloyed with Au [39].For example, when the UPL is kept lower than the Pd dissolution onset potential, i.e. under ADP-0.8, the shape of the CV is maintained even after 1000 degradation cycles.

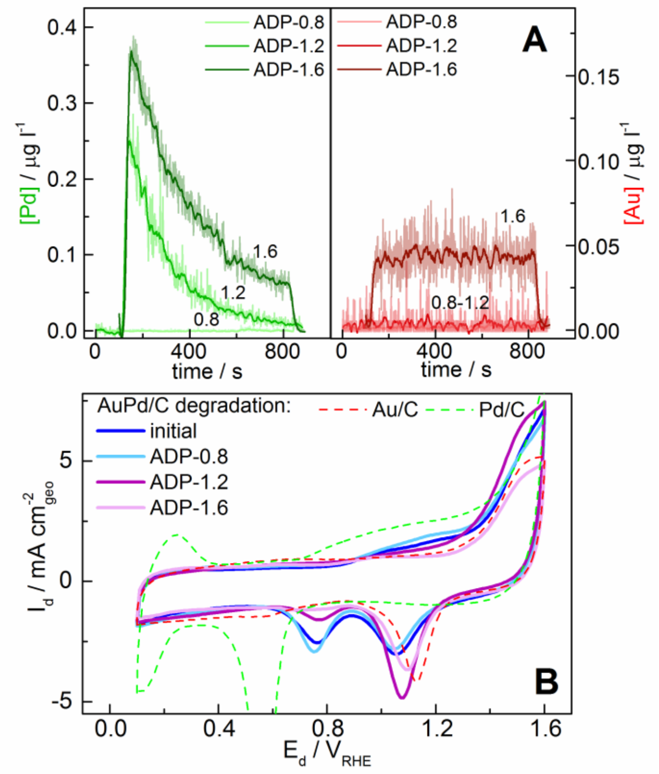

Figure 1 (a) Online Pd and Au dissolution profiles recorded with AuPd/C means SFC/ICPMS technique during degradation cycle voltammogramms [0.1-UPL] V_{RHE}. (b) Initial AuPd/C CV [0.1-1.6] V_{RHE} in Ar purged 0.1M $HClO_4$, as well as after degradation protocols (1000CV 0.8 V_{RHE}, 1000CV 1.2 V_{RHE}, 100CV 1.6 V_{RHE}). As a reference the Au/C and Pd/C CVs are also shown. Scan rates: 0.2 V s^{-1}.

Table 1 Potential and charge associated to the Pd-O and Au-O reduction peaks corresponding to the Ar background CVs recorded after degradation.

AuPd/C	Pd-O reduction		Au-O reduction	
	E_d (V_{RHE})	Q (mC)	E_d (V_{RHE})	Q (mC)
Initial	0.75	0.17	1.05	0.29
ADP-0.8	0.76	0.19	1.05	0.27
ADP-1.2	0.77	0.06	1.07	0.5
ADP1.6		<0.01	1.09	0.36

Nevertheless, the charge associated to Pd reduction peak appears to be slightly larger after degradation ADP-0.8 (Figure S1). As no significant dissolution is occurring during such ADP, the difference can be tentatively attributed to a dynamic change in the nanoparticle structure during potential cycling. Indeed, DFT and experimental studies suggest catalyst surface rearrangement or “breathing”, i.e. Pd surface segregation with absorbed H_2 [41,42], O_2 [22] or CO [43-45] in addition to Au migration towards the surface during catalytic [46] and electrocatalytic [29] measurements. As the potential exceeds the Pd dissolution, the charge associated with the Pd reduction is decreasing during CVs under both ADP-1.2 and ADP-1.6 (Figure S2,S3).

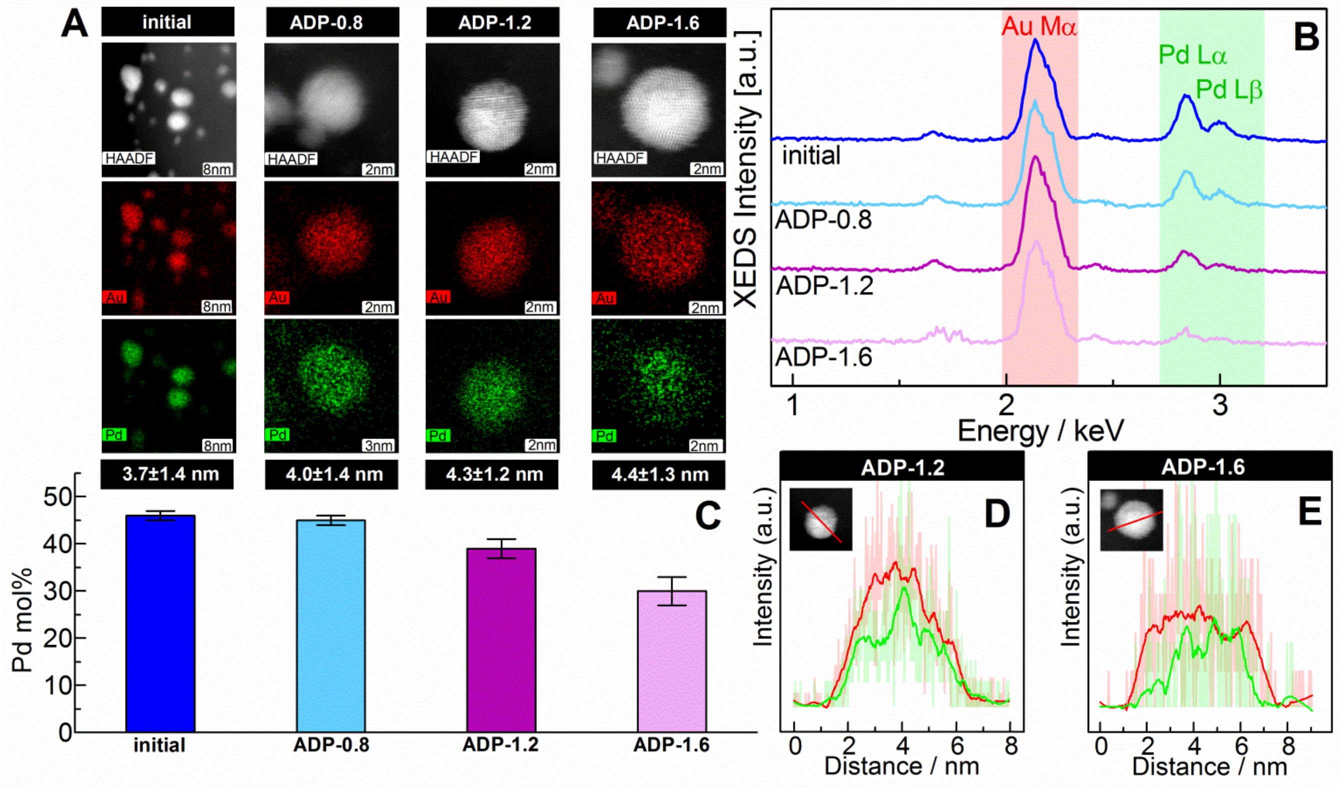

Figure 2 (a) High angle annular dark-field scanning transmission electron microscopy (HAADF-STEM) investigation of AuPd/C before (initial) and after degradation protocols (1000CV 0.8 V_{RHE}, 1000CV 1.2 V_{RHE}, 100CV 1.6 V_{RHE}) is shown in first row. The STEM-EDS elemental maps of Au and Pd are shown in row 2 and 3. The average particle size is reported as well (bright field micrographs as well as the particle size distributions histograms of identical locations before and after the aforementioned treatment are shown in the SI). (b) Corresponding energy dispersive spectra normalized to the Au-M peak. (c) Pd% molar ratio ($mol_{Pd}/(mol_{Pd}+mol_{Au})$) before and after degradation measured by post-mortem analysis with the ICPMS. (d-e) Catalyst EDS line scan after degradation (1000CV 1.2 V_{RHE} and 100CV 1.6 V_{RHE}).

After only 100 CV under ADP-1.6 the reduction peak fully disappears, whereas after 1000 CV under ADP-1.2 still the reduction peak is observed (see CV in Figure 1b). This suggests that Pd is still present on the surface despite 1000 CV cycles at ADP-1.2.

Nevertheless, it needs to be considered that this reduction peak was suggested to be associated to a new surface phase of alloyed Au and Pd [39]. With this consideration, Pd could still be present under a surface consisting of mainly Au and in this case the observed reduction peak might be attributed to surface Au alloyed with underlying Pd. However, we would exclude this as such feature is not observed in core-shell configuration (with a Au-shell) [39]. We suggest here that there is some dispersed Pd on the surface which is not further dissolving thanks to the presence of Au that might stabilize it, as elsewhere suggested for Pt [36]. As expected during Pd leaching, the surface concentration of Au increases [29,39,47] as observed from the associated reduction peak (Figure 1b).

The Au reduction peak after ADP-1.6 is lower than after ADP-1.2 as Au is dissolving under ADP-1.6 (see also the Au reduction peak evolution under ADP-1.6 in Figure S3). For a more detailed investigation on Au-Pd catalyst surface changes (and the relative changes in CVs) we invite the reader to refer to the work of *Lukaszewski et al.* [39]. In their study, the influence of the electrochemical protocol, of the initial alloy composition as well of hydrogen absorption or oxygen electrochemisorption is discussed.

3.2 EVOLUTION OF CATALYST STRUCTURE AND COMPOSITION

Electrochemistry is a powerful tool to study the macroscopic changes of the catalyst changes in the argon background CVs, as discussed in the previous section, that correlate to changes in the catalyst surface state and composition. Microstructural changes were characterized with TEM (Figure 2 and S4-S6). The initial theoretical composition of AuPd/C is confirmed both by EDS elemental map (47 Pd mol%) and ICP-MS bulk analysis (46±1 Pd mol%), while STEM-EDS mapping indicates homogeneous Pd and Au distribution within the nanoparticles (Figure 2a). Identical location TEM (IL-TEM) is able to compare the same catalyst area before and after degradation, thus allowing a clearer description of the catalyst degradation mechanisms on the nanoscale [35]. In this study, the change in particle size distribution as well as overall number of particle counts are recorded through IL-TEM before, after 100 CVs and after 1000 CVs of the three ADPs (Figure S4-S6). After ADP-0.8 (Figure S4) no major change in the particle size distribution and in the overall number of particles are observed (the small increase in mean particle size from 3.7 to 4.0 nm can be observed due to minor agglomeration). For ADP-1.2 and ADP-

1.6 after 100 CVs the number of particle counts on the identical location dropped by 30-50% as a consequence of dissolution and detachment. Furthermore, the collected IL-TEM images suggest that the average particle size increases from 3.8 to 4.4 nm and from 3.5 to 4.4 nm for ADP-1.2 and ADP-1.6 respectively due to a decrease in number of particles with sizes below ~3 nm (Figure S5,S6). For such ADPs, this increase, as well as the particle rounding) can be attributed to potential induced metal dissolution/dealloying and consequent Ostwald ripening [48,49]. Interestingly, comparing the IL-TEM micrographs after 100 CVs and 1000 CVs of ADP-1.2, the number of particle counts as well as the average size remains unchanged. In this case, clearly, the Au dissolution is excluded whereas Pd dissolution/dealloying decreases below the ICP-MS detection limit (Figure 1a) as the surface is enriched in Au. Therefore, either Au is stabilizing the remaining Pd as claimed in literature [36,50] or a protective Au shell is preventing further dealloying as already observed in the case of Pt based alloys [51-53]. Giving the relevance of knowing the spatial distribution of the alloying elements of AuPd/C, additional high resolution STEM-EDS analysis of single nanoparticles are acquired after the ADPs (Figure 2a-b) and the overall composition is obtained with post-mortem analysis with ICPMS (Figure 2c). In agreement with the online ICP-MS results, upon ADP-0.8 the metal atoms are still homogeneously distributed within the catalyst and the Pd molar ratio (defined as $mol_{Pd}/(mol_{Pd}+mol_{Au})$) is 45±1 mol%, within the error compared to the initial composition. Increasing the UPL, the Pd molar ratio (Figure 2c) decreases after 100 CVs to 41±1 and 30±3 mol% for ADP-1.2 and ADP-1.6 respectively (a trend also confirmed by the decrease in Pd Lα and Lβ of the respective EDS spectra in Figure 2b). Upon additional 900 cycles of ADP-1.2 the measured Pd molar ratio is 39±2 mol% (average after 3 separate degradation measurements), indicating that the further dealloying is almost negligible. Clearly, under ADP-1.2 a quasi-stable configuration, for which no changes in composition and structure occurs, is obtained after few potential cycles.

The EDS line scans after ADP-1.2 (Figure 2d) indicate that while the core is still homogeneous (Pd and Au intensity heights are equal as expected by the initial composition), the Pd content at the surface is lower but seemingly still present. Indeed, in this case an evident formation of core-shell nanoparticles was not observed. Note however, that a precise visualization of the molar surface composition is rather challenging due to the small size of the nanoparticle, which can be susceptible to beam damage. Some monomer or small Pd clusters stabilized by the surrounding Au might be therefore still present on the surface but the surface composition is very Au rich (as also indicated by the small Pd-O reduction peak in Figure 1b). On the other hand, the EDS line scans after ADP-1.6 (Figure 2e) clearly establish the presence of a AuPd core (similar Pd and Au intensities) surrounded by a Au shell (0.5-1 nm thickness). When the UPL exceeds the threshold for significant Au dissolution this shell is destabilized and the dissolution of Pd from the core of the nanoparticles is initiated, causing further de-alloying as observed also for Pt based catalyst [51].

3.3 CONSEQUENCES FOR THE TIME EVOLUTION OF H_2O_2 SELECTIVITY

In the previous sections, we described the surface composition and nanostructural changes due to the dissolution and catalyst degradation under the three considered ADPs. In this section, we study how these changes are actually influencing the oxygen reduction reaction (ORR) performance. In particular, we focus on the H_2O_2 production and selectivity measured with the RRDE techniques (Figure 3). The measured disc current (I_d), ring currents (I_r) as well as the calculated selectivity (S_{H2O2}) are shown in Figure 3a,b,c respectively. As a reference, also the RRDE results for Au/C and Pd/C are reported here. The estimated mean particle diameters (determined by TEM) of the as prepared catalysts are 4.5±1 nm, 3.7±1.4 nm, 4.0±0.8 nm for Au/C, AuPd/C and Pd/C respectively.

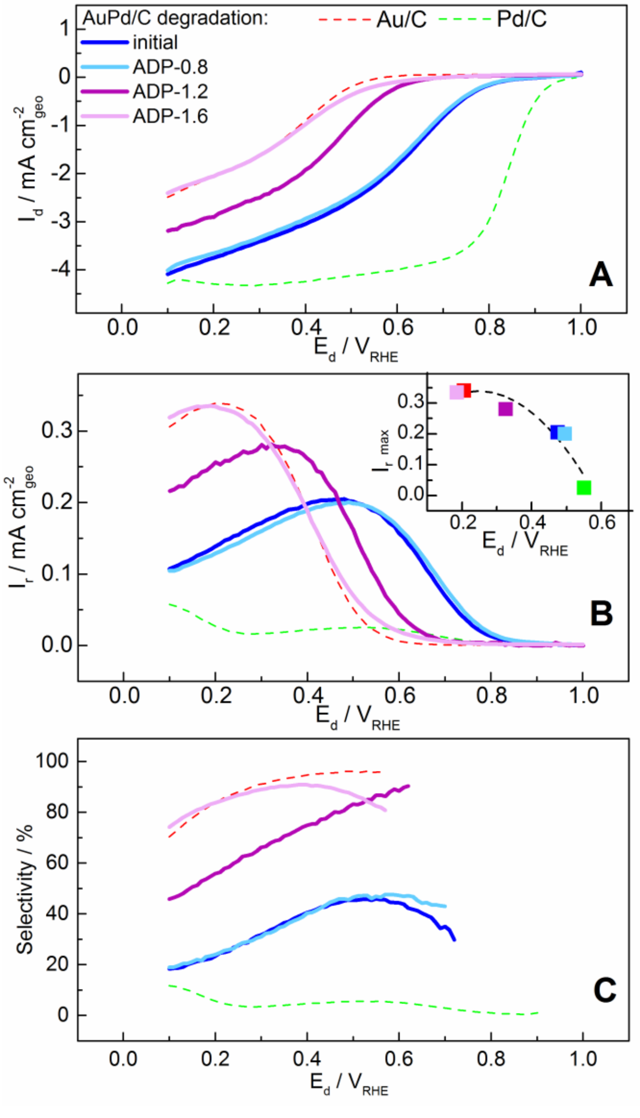

Figure 3 Collection of the ORR results (I_d in (a), I_r in (b) and selectivity in (c)) obtained with RRDE in O_2 saturated 0.1M $HClO_4$ for the AuPd/C before as well as after degradation protocols (ADP-0.8, ADP-1.2, ADP-1.6). As a reference, the Au/C and Pd/C CVs are also shown. Rotation: 900 rpm. Scan rate: 0.05 V s^{-1}. E_r: 1.0 $V_{Ag/AgCl}$.

Owing to the similar average particle size and a narrow distribution, the total surface area is expected to be in the same range. Nevertheless, we normalize the currents here to the geometric surface area (0.196 cm^2), as the real surface area of AuPd is expected to change significantly following the catalyst degradation. The pure metal catalysts (Au/C and Pd/C) provide frames between an almost pure 2-electron behavior of Au [23,54-56] and a 4-electron behavior of Pd [17,18,57,58]. In our previous publication [23] the S_{H2O2} of both unsupported Au nanoparticles and polycrystalline Au was 95% and independent of the applied potential, whereas the S_{H2O2} of Vulcan supported Au/C increases from around 80-85% at 0.1 V_{RHE} to almost 100% at higher potentials (see also a comparison in Figure S7). This potential dependence was observed also by *Jirkovski et al.* [15,21] and it might be related to the presence of the carbon support, as they showed a selectivity decrease with layer thickness. The initial ORR behavior of the alloyed catalyst (AuPd/C) was also described earlier [23,37,59]. The shift in ORR onset potential and the change in H_2O_2 current with respect to the pure metal counterparts was attributed to a change in mechanism, as the electronic structure changes in the alloy in dependence of the spatial Au and Pd atom distribution [21]. In this case, a maximum of 40-45% in S_{H2O2} of the initial AuPd/C is observed at ca. 0.5 V_{RHE}. Despite the lower S_{H2O2} compared to pure Au, the alloyed metal is much more active and the overpotential for the ORR to H_2O_2 is therefore significantly lower. Thus, it can be considered as a good candidate for the electrocatalytic on-site production for those applications for which low H_2O_2 concentration in H_2O is required. Under ADP-0.8, no relevant changes, besides a negligible shift of the onset potential, are observed (Figure 3 and S8), whereas significant changes occur under ADP-1.2 and ADP-1.6. In Figure 3 the last positive sweeps after degradation (1000 CVs of ADP-0.8 and ADP-1.2 and 100 CVs of ADP-1.6) are shown and intermediate positive sweeps are illustrated in the SI. When only Pd is dissolving (ADP-1.2) the onset potential is shifted by ~200 mV after only 10 CVs (Figure S9). Upon further potential cycling the ORR onset potential as well as the H_2O_2 current onset potential stabilize around 0.7 V_{RHE} and the I_d and I_r do not change significantly between 50 and 1000 CVs. It seems that under such conditions the initial performance degradation are followed by a "stable" state, which is still more active than pure Au and more selective than the initial AuPd/C (70% at the potential of maximum I_r). From this state on no further degradation is observed, unless the UPL is raised. For instance, under ADP-1.6 already after 10 CVs the onset potential is shifted by ~300 mV (Figure S10). After 100 CVs the degraded catalyst behaves very similar to Au/C (Figure 3), while the onset potential still remains slightly higher than pure Au. This can be attributed to the alloying effect of Pd that is still present in the core, as it was abundantly reported for dealloyed Pt-M alloys with a Pt skin [52,60-63].

The trend of the selectivity (S_{H2O2} in Figure 3c) and of the ring current maxima ($I_{r,max}$ in the inset of Figure 3b) visually summarize the results obtained with the RRDE. The potential shift can be attributed to the change in surface composition described in the previous sections. The UPL-dependent evolution of the AuPd alloy surface composition under the considered ADPs is schematically represented in Scheme 1, indicating the formation of a core shell depending on the applied UPL.

The surface reactivity and H_2O_2 selectivity at the potential of maximum I_r (indicated by the percentage values) follow the surface composition evolution. The change in particle size is also reported and it is attributed to the re-deposition of dissolved metals (Ostwald ripening) as well as to particle agglomeration.

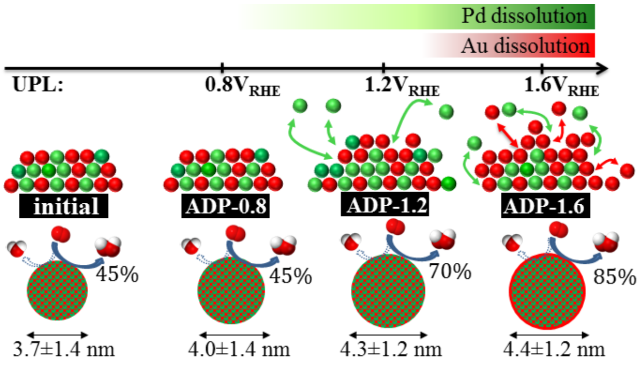

Scheme 1 Representative evolution of the surface composition and of the H_2O_2 selectivity (% values) during the ADPs.

4 CONCLUSION

In this work, we investigate the structural changes of carbon supported Au, Pd, and AuPd/C catalysts. Three different potential degradation conditions are chosen with the aim to distinguish the degradation processes that might affect performance, namely below the Pd/Au dissolution onset potentials (ADP-0.8), above the Pd but below the Au dissolution potentials (ADP-1.2), and above the Au/Pd dissolution potentials (ADP-1.6). The associated chemical and structural changes are then related to the H_2O_2 electrochemical production and selectivity. While under ADP-0.8 the catalyst and its electrochemical behavior are unchanged, above the Pd dissolution potential (ADP-1.2) the surface composition changes, becoming enriched in Au. In this case, Pd surface de-alloying did not result in an evident core-shell configuration. As the Au does not dissolve, further Pd dissolution is prevented and a "stable" state is obtained, for which no further electrochemical changes are observed. As a result, the catalyst still remains more active than pure Au/C and more selective than the initial AuPd/C. When the UPL is high enough to induce Au dissolution and redeposition (ADP-1.6) in parallel to a significant Pd dissolution, the catalyst degradation results in an alloyed core surrounded by a Au shell. Thus, the behavior approaches the one of pure Au, although the alloying effect of Pd still present in the core induces a small shift in the ORR onset potential.

For the first time, this study correlates the catalyst degradation with the H_2O_2 selectivity using AuPd as a model catalyst. The conclusions are particularly important and can be extended to similar bimetallic catalysts (as Au-Pd, Hg-Pd, HgPt…), which are considered promising for the on-site electrocatalytic H_2O_2 production in fuel cells or other related electrochemical reactions. Indeed, sudden potential changes or spikes, recurring during start-stop of fuel cells, can induce significant surface composition changes within few cycles that might substantially change the electrochemical behavior. Dedicated strategies either in catalyst material design or in control of operational conditions have to be considered for an effective employment of a direct H_2O_2 synthesis approach. More generally, the work emphasizes the importance of fundamental long term stability investigations for complex electrochemical reactions where selectivity is a crucial performance indicator.

AUTHOR INFORMATION

Corresponding Author

* pizzutilo@mpie.de, mayrhofer@mpie.de
Tel.: +49 211 6792 160, FAX: +49 211 6792 218).

Author Contributions

The manuscript was written through contributions of all authors. All authors have given approval to the final version of the manuscript.

ASSOCIATED CONTENT

Supporting Information. Background CV before and after the ADP. IL-TEM. ORR behavior and peroxide selectivity during the degradation.

ACKNOWLEDGMENT

E.P acknowledges financial support from the IMPRS-SurMat doctoral program. We thank the MAXNET Energy for the financial support. We acknowledge Simon Geiger for his contribution on the SFC-ICPMS measurement.

ABBREVIATIONS

PEMFC, proton exchange membrane fuel cells; ICPMS, inductively coupled plasma mass spectrometry; IL-TEM, identical location transmission electron microscope; HAADF-STEM/EDS, High angle annular dark-field scanning transmission electron microscope/energy dispersive spectroscopy; UPW, ultrapure water; RHE, reversible hydrogen electrode; WE, working electrode; CE, counter electrode; RE, reference electrode; GC, glassy carbon; RRDE, rotating ring disc electrode; ORR, oxygen reduction reaction; PROR, peroxide reduction and oxidation reaction; ADP, accelerated degradation protocol; SFC, scanning flow cell; UPL, upper potential limit; CV, cyclic voltammogram.

REFERENCES

(1) Zellmer, L. *Libr J* **2007**, *132*, 158-158.

(2) Riedl, H.; Pfleiderer, G. *US Patent 2158525* **1939**.

(3) Edwards, J. K.; Freakley, S. J.; Lewis, R. J.; Pritchard, J. C.; Hutchings, G. J. *Catal Today* **2015**, *248*, 3-9.

(4) Campos-Martin, J. M.; Blanco-Brieva, G.; Fierro, J. L. G. *Angew Chem Int Edit* **2006**, *45*, 6962-6984.

(5) Edwards, J. K.; Solsona, B.; N, E. N.; Carley, A. F.; Herzing, A. A.; Kiely, C. J.; Hutchings, G. J. *Science* **2009**, *323*, 1037-1041.

(6) Choudhary, V. R.; Gaikwad, A. G.; Sansare, S. D. *Catal Lett* **2002**, *83*, 235-239.

(7) Enache, D. I.; Edwards, J. K.; Landon, P.; Solsona-Espriu, B.; Carley, A. F.; Herzing, A. A.; Watanabe, M.; Kiely, C. J.; Knight, D. W.; Hutchings, G. J. *Science* **2006**, *311*, 362-365.

(8) Fellinger, T. P.; Hasche, F.; Strasser, P.; Antonietti, M. *J Am Chem Soc* **2012**, *134*, 4072-4075.

(9) Alcaide, F.; Brillas, E.; Cabot, P. L. *J Electrochem Soc* **1998**, *145*, 3444-3449.

(10) Brillas, E.; Alcaide, F.; Cabot, P. L. *Electrochim Acta* **2002**, *48*, 331-340.

(11) Yamanaka, I.; Onizawa, T.; Takenaka, S.; Otsuka, K. *Angew Chem Int Edit* **2003**, *42*, 3653-3655.

(12) Yamanaka, I.; Tazawa, S.; Murayama, T.; Iwasaki, T.; Takenaka, S. *Chemsuschem* **2010**, *3*, 59-62.

(13) Yamanaka, I.; Onisawa, T.; Hashimoto, T.; Murayama, T. *Chemsuschem* **2011**, *4*, 494-501.

(14) Yamanaka, I.; Onizawa, T.; Suzuki, H.; Hanaizumi, N.; Nishimura, N.; Takenaka, S. *J Phys Chem C* **2012**, *116*, 4572-4583.

(15) Jirkovsky, J. S.; Halasa, M.; Schiffrin, D. J. *Phys Chem Chem Phys* **2010**, *12*, 8042-8052.

(16) Sanchez-Sanchez, C. M.; Bard, A. J. *Anal Chem* **2009**, *81*, 8094-8100.

(17) Antolini, E. *Energ Environ Sci* **2009**, *2*, 915-931.

(18) Antolini, E.; Zignani, S. C.; Santos, S. F.; Gonzalez, E. R. *Electrochim Acta* **2011**, *56*, 2299-2305.

(19) Markovic, N. M.; Gasteiger, H. A.; Ross, P. N. *J Phys Chem-Us* **1995**, *99*, 3411-3415.

(20) Gasteiger, H. A.; Markovic, N. M. *Science* **2009**, *324*, 48-49.

(21) Jirkovsky, J. S.; Panas, I.; Ahlberg, E.; Halasa, M.; Romani, S.; Schiffrin, D. J. *J Am Chem Soc* **2011**, *133*, 19432-19441.

(22) Jirkovsky, J. S.; Panas, I.; Romani, S.; Ahlberg, E.; Schiffrin, D. J. *J Phys Chem Lett* **2012**, *3*, 315-321.

(23) Pizzutilo, E.; Kasian, O.; Choi, C. H.; Cherevko, S.; Hutchings, G. J.; Mayrhofer, K. J. J.; Freakley, S. J. *Chemical Physics Letters* **2017**, *683*, *436-442*.

(24) Siahrostami, S.; Verdaguer-Casadevall, A.; Karamad, M.; Deiana, D.; Malacrida, P.; Wickman, B.; Escudero-Escribano, M.; Paoli, E. A.; Frydendal, R.; Hansen, T. W.; Chorkendorff, I.; Stephens, I. E. L.; Rossmeisl, J. *Nat Mater* **2013**, *12*, 1137-1143.

(25) Siahrostami, S.; Verdaguer-Casdevall, A.; Karamad, M.; Chorkendorff, I.; Stephens, I.; Rossmeisl, J. *Electrochemical Synthesis of Fuels 2* **2013**, *58*, 53-62.

(26) Verdaguer-Casadevall, A.; Deiana, D.; Karamad, M.; Siahrostami, S.; Malacrida, P.; Hansen, T. W.; Rossmeisl, J.; Chorkendorff, I.; Stephens, I. E. L. *Nano Lett* **2014**, *14*, 1603-1608.

(27) Borup, R.; Meyers, J.; Pivovar, B.; Kim, Y. S.; Mukundan, R.; Garland, N.; Myers, D.; Wilson, M.; Garzon, F.; Wood, D.; Zelenay, P.; More, K.; Stroh, K.; Zawodzinski, T.; Boncella, J.; McGrath, J. E.; Inaba, M.; Miyatake, K.; Hori, M.; Ota, K.; Ogumi, Z.; Miyata, S.; Nishikata, A.; Siroma, Z.; Uchimoto, Y.; Yasuda, K.; Kimijima, K. I.; Iwashita, N. *Chem Rev* **2007**, *107*, 3904-3951.

(28) Kocha, S. S. *Polymer Electrolyte Fuel Cell Degradation* **2012**, 89-214.

(29) Brodsky, C. N.; Young, A. P.; Ng, K. C.; Kuo, C. H.; Tsung, C. K. *Acs Nano* **2014**, *8*, 9368-9378.

(30) Pizzutilo, E.; Freakley, S.; Geiger, S.; baldizzone, c.; Mingers, A.; Hutchings, G.; Mayrhofer, K. J. J.; Cherevko, S. *Catalysis Science & Technology* **2017**, *7*, 1848-1856.

(31) Pizzutilo, E.; Geiger, S.; Freakley, S. J.; Mingers, A.; Cherevko, S.; Hutchings, G. J.; Mayrhofer, K. J. J. *Electrochim Acta* **2017**, *229*, 467-477.

(32) Pizzutilo, E.; Geiger, S.; Grote, J.-P.; Mingers, A.; Mayrhofer, K. J. J.; Arenz, M.; Cherevko, S. *J Electrochem Soc* **2016**, *163*, F1510-F1514.

(33) Koh, S.; Strasser, P. *J Am Chem Soc* **2007**, *129*, 12624-12625.

(34) Cherevko, S.; Topalov, A. A.; Katsounaros, I.; Mayrhofer, K. J. J. *Electrochem Commun* **2013**, *28*, 44-46.

(35) Mezzavilla, S.; Cherevko, S.; Baldizzone, C.; Pizzutilo, E.; Polymeros, G.; Mayrhofer, K. J. J. *ChemElectroChem* **2016**, *3*, 1524-1536.

(36) Gatalo, M.; Jovanovič, P.; Polymeros, G.; Grote, J.-P.; Pavlišič, A.; Ruiz- Zepeda, F.; Šelih, V. S.; Šala, M.; Hočevar, S.; Bele, M.; Mayrhofer, K. J. J.; Hodnik, N.; Gaberšček, M. *Acs Catal* **2016**, *6*, 1630-1634.

(37) Erikson, H.; Sarapuu, A.; Kozlova, J.; Matisen, L.; Sammelselg, V.; Tammeveski, K. *Electrocatalysis-Us* **2015**, *6*, 77-85.

(38) Grdeń, M.; Łukaszewski, M.; Jerkiewicz, G.; Czerwiński, A. *Electrochim Acta* **2008**, *53*, 7583-7598.

(39) Lukaszewski, M.; Czerwinski, A. *Electrochim Acta* **2003**, *48*, 2435-2445.

(40) Lukaszewski, M.; Kusmierczyk, K.; Kotowski, J.; Siwek, H.; Czerwinski, A. *J Solid State Electr* **2003**, *7*, 69-76.

(41) Okube, M.; Petrykin, V.; Mueller, J. E.; Fantauzzi, D.; Krtil, P.; Jacob, T. *Chemelectrochem* **2014**, *1*, 207-212.

(42) Venkatachalam, S.; Jacob, T. *Phys Chem Chem Phys* **2009**, *11*, 3263-3270.

(43) Gao, F.; Wang, Y. L.; Goodman, D. W. *J Phys Chem C* **2009**, *113*, 14993-15000.

(44) Hahn, C.; Abram, D. N.; Hansen, H. A.; Hatsukade, T.; Jackson, A.; Johnson, N. C.; Hellstern, T. R.; Kuhl, K. P.; Cave, E. R.; Feaster, J. T.; Jaramillo, T. F. *J Mater Chem A* **2015**, *3*, 20185-20194.

(45) Soto-Verdugo, V.; Metiu, H. *Surf Sci* **2007**, *601*, 5332-5339.

(46) Alayoglu, S.; Tao, F.; Altoe, V.; Specht, C.; Zhu, Z. W.; Aksoy, F.; Butcher, D. R.; Renzas, R. J.; Liu, Z.; Somorjai, G. A. *Catal Lett* **2011**, *141*, 633-640.

(47) Rand, D. A. J.; Woods, R. *J Electroanal Chem* **1972**, *36*, 57-69.

(48) Rasouli, S.; Ortiz Godoy, R. A.; Yang, Z.; Gummalla, M.; Ball, S. C.; Myers, D.; Ferreira, P. J. *J Power Sources* **2017**, *343*, 571-579.

(49) Ahluwalia, R. K.; Arisetty, S.; Peng, J.-K.; Subbaraman, R.; Wang, X.; Kariuki, N.; Myers, D. J.; Mukundan, R.; Borup, R.; Polevaya, O. *J Electrochem Soc* **2014**, *161*, F291-F304.

(50) Sasaki, K.; Naohara, H.; Choi, Y. M.; Cai, Y.; Chen, W. F.; Liu, P.; Adzic, R. R. *Nat Commun* **2012**, *3*, 1115-1124.

(51) Mezzavilla, S.; Baldizzone, C.; Swertz, A.-C.; Hodnik, N.; Pizzutilo, E.; Polymeros, G.; Keeley, G. P.; Knossalla, J.; Heggen, M.; Mayrhofer, K. J. J.; Schüth, F. *Acs Catal* **2016**, 8058-8068.

(52) Gan, L.; Heggen, M.; Rudi, S.; Strasser, P. *Nano Lett* **2012**, *12*, 5423-5430.

(53) Rasouli, S.; Fujigaya, T.; Myers, D.; Nakashima, N.; Ferreira, P. *Microscopy and Microanalysis* **2016**, *22*, 1358-1359.

(54) Guerin, S.; Hayden, B. E.; Pletcher, D.; Rendall, M. E.; Suchsland, J. P. *J Comb Chem* **2006**, *8*, 679-686.

(55) Rodriguez, P.; Koper, M. T. M. *Phys Chem Chem Phys* **2014**, *16*, 13583-13594.

(56) Markovic, N. M.; Adzic, R. R.; Vesovic, V. B. *J Electroanal Chem* **1984**, *165*, 121-133.

(57) Jiang, L.; Hsu, A.; Chu, D.; Chen, R. *J Electrochem Soc* **2009**, *156*, B643-B649.

(58) Kondo, S.; Nakamura, M.; Maki, N.; Hoshi, N. *J Phys Chem C* **2009**, *113*, 12625-12628.

(59) Damjanovic, A.; Brusic, V. *Electrochim Acta* **1967**, *12*, 1171-1184.

(60) Hasche, F.; Oezaslan, M.; Strasser, P. *Chemcatchem* **2011**, *3*, 1805-1813.

(61) Mani, P.; Srivastava, R.; Strasser, P. *J Power Sources* **2011**, *196*, 666-673.

(62) Strasser, P.; Koh, S.; Anniyev, T.; Greeley, J.; More, K.; Yu, C. F.; Liu, Z. C.; Kaya, S.; Nordlund, D.; Ogasawara, H.; Toney, M. F.; Nilsson, A. *Nat Chem* **2010**, *2*, 454-460.

(63) Stamenkovic, V. R.; Mun, B. S.; Mayrhofer, K. J. J.; Ross, P. N.; Markovic, N. M. *J Am Chem Soc* **2006**, *128*, 8813-8819.

Insert Table of Contents artwork here